A Multi-Physics Design Methodology Applied to a High-Force-Density Short-Duty Linear Actuator

N. Simpson, R. Wrobel and P. H. Mellor
Department of Electrical and Electronic Engineering
University of Bristol
Bristol, UK
nick.simpson@bristol.ac.uk

***Abstract*—This paper presents a coupled electromagnetic and thermal design methodology which addresses the problem of balancing accuracy against computation time. A case study on a short-duty permanent magnet linear actuator is used to illustrate the approach. The proposed method employs a two-dimensional electromagnetic finite element model coupled with a detailed thermal equivalent circuit model which is automatically constructed and parameterised using geometric and material data. A numerical method of estimating the equivalent thermal properties of the winding amalgam is used along with published empirically derived convection and radiation heat transfer correlations. The relatively high number of network nodes and more accurate thermal material properties minimise model calibration and allows improved temperature prediction, including winding hot-spots, whilst maintaining a low computational cost for both steady-state and transient analyses. A comparison between experimental and theoretical actuator performance shows that the design methodology provides good accuracy electromagnetic and transient thermal performance predictions without the need for direct model calibration and can yield an optimised design within an acceptable time-frame.**

***Index Terms*—short-duty, transient, coupled model, design methodology, electromagnetic, thermal, optimisation, linear permanent-magnet (PM) actuator, thermal equivalent circuit (TEC), lumped parameter (LP), material property estimation**

I. Introduction

The desire for electrical machines and devices to meet evermore demanding specifications in terms of power-density, energy-efficiency and short-duty operation, requires electromagnetic, thermal and other relevant physical phenomena to be accounted for simultaneously at the design stage, [1], through the use of coupled multi-physics design methodologies employing combinations of analytical, [2], [3], lumped parameter, [4], [5] and numerical, [3], [5]–[7], modelling techniques along with appropriate optimisation routines, [3], [8]. A major limiting factor on the energy conversion capability of such electrical machines and devices is the ability to dissipate internally generated heat and, in turn, the temperature rating of the electrical insulation system and permanent magnets (PMs), if present. Therefore, in the design of high-performance machines and devices the electromagnetic and thermal phenomena should be accounted for, at a minimum, in order to allow a greater exploitation of materials and yield more compact and lighter designs.

An ideal coupled electromagnetic and thermal analysis technique would consist of detailed physical models, fully representative of the device geometry and materials, which iteratively exchange generated loss and temperature information to yield an accurate prediction of the electromagnetic and thermal performance. This coupled analysis could then be incorporated into an optimisation procedure in order to iteratively steer the design variables to meet a desired specification. However, without proper selection of the modelling methods, model coupling, methodology structure and optimisation routine, the computation time of such an approach can often be prohibitive. This limitation is typically addressed by one or more of the following methods, [2]–[4], [6]–[9]:

- make simplifying assumptions
- reduce the modelling domain by exploiting symmetry
- select the most beneficial modelling techniques for the application
- use surrogate models
- reduce the number of model evaluations through proper selection of the design methodology structure
- loosely couple the models
- compromise the accuracy and detail of the models in favour of low computation time so as to ensure the feasibility of the design methodology

The selection of modelling methods and design methodology structure are application specific and therefore difficult to generalise, as evidenced by the various approaches taken in the literature, [3], [4], [6]–[9]. However, a common approach links a relatively detailed electromagnetic Finite Element (FE) model with a coarse low computational cost Thermal Equivalent Circuit (TEC) model, [3], [4], [6], [8], [9].

The computation time of the electromagnetic FE model can be tailored by careful selection of the various mesh densities, by modifying the level of model detail, for example, representing the individual conductors within a winding by a lumped homogeneous region with an equivalent current density, or by employing computationally efficient FE techniques to infer the information required using a minimum number of FE model evaluations, [9].

The TEC models are often manually constructed based on experience and as such contain only a few nodes. This affords short solution times for both steady and transient analyses, however, the small number of nodes tends to compromise thermal field detail and solution accuracy if a calibration

procedure based on experimental observations is not used. This process can be time consuming or even infeasible if a prototype or device similar to that under consideration is not readily available.

In this paper, a coupled analysis composed of a two-dimensional electromagnetic FE model loosely coupled with a detailed TEC model which is automatically constructed and parameterised using geometric and material data is proposed, [10]. A numerical method of estimating the equivalent thermal properties of the winding amalgam is used to inform the thermal model, [11], along with published empirically derived convection and radiation heat transfer correlations. The relatively high number of network nodes and more accurate thermal model parameters enable improved accuracy transient temperature predictions, including winding hot-spots, without the need for direct thermal model calibration. The loose coupling of the physical models is exploited to enable parallel model evaluation resulting in a comparatively low computation time multi-physics analysis, which, when paired with an optimisation routine, can yield a specification optimised design within an acceptable time-frame using modern desktop computing hardware. The method is applied to the design of a short-duty, high-force-density linear actuator, experimental results from which are used to illustrate and validate the approach.

II. Specification of Actuator Case Study

The specification of the single phase PM tubular linear actuator, [12], [13], is summarised in Table I and a cross section of the actuator topology with four stator slots, N_s, and four effector poles, N_p, is illustrated in Fig. 1. The actuator is required to provide an average thrust force, F, of ≥ 1.5 kN over an effector displacement, dz, of 5 mm for a minimum duration, t, of 30 seconds and remain below the maximum operating temperature of the electrical insulation system, T_{max}, of 180 °C at the hottest spot. It is important to note that the actuator is assumed to operate in an environment with an ambient temperature of $T_0 = 25$ °C and the nature of the application requires the actuator to be cooled by natural convection to the ambient temperature between each actuation event. The maximum duty ratio of the system is governed by other components (not considered here) with a significantly greater thermal time constant than that of the actuator. In the present study the dynamic behaviour such as the force response time is not considered. The actuator operation can be characterised as dc, however, in order to simplify manufacturing and minimise ac eddy current loss arising in future force control development, a Somaloy 700 Soft Magnetic Composite (SMC) prototyping material is selected. However, the relatively low permeability and high cost of the prototyping material can negatively impact performance and cost-effectiveness, hence, the use of solid or laminated electrical steels could be explored in future work, [14]. The effector is assumed to be of an Interior Permanent Magnet (IPM) configuration due to the ease of construction and comparative low cost, [15]. The actuator stator is restricted to a space envelope of 764 cm^3, Table I. In order to simplify the machining process, the tooth tips are not tapered, Fig. 1. Samarium-Cobalt (SmCo) PMs are favoured over Neodymium (NdFeB) types due to their superior high temperature performance. The cogging force occurring between the PMs and the slotted stator is exploited to provide a restoring force on the effector when the windings are not energised.

TABLE I
Actuator specification

Parameter	Value	Unit
Stator radius, R_{so}	45	mm
Stator length, L_{so}	120	mm
Effector displacement, dz	5	mm
Mechanical air-gap, dr_{ag}	0.5	mm
Thrust force, F	1.5	kN
Thrust duration, t	30	s
Maximum winding temperature, T_{max}	180	°C

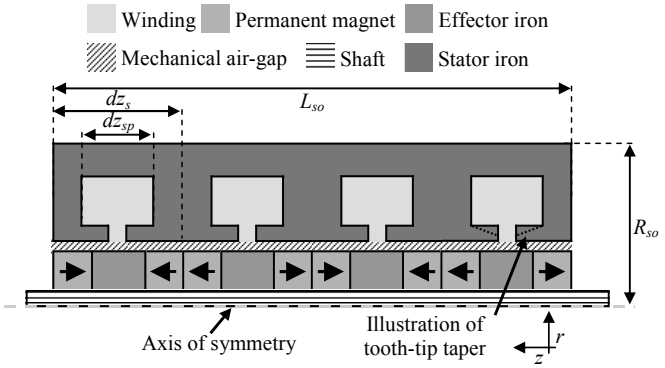

Fig. 1. Actuator cross section geometry (axisymmetric).

III. Electromagnetic Modelling

The actuator stator is geometrically constrained and slotted, which makes local saturation, slotting and end effects significant, therefore the well known numerical non-linear FE modelling method is favoured over analytical approaches, [16]–[18]. The quasi-static operation and rotational symmetry of the actuator allow a parametrically defined magnetostatic axisymmetric model to be adopted, [19].

IV. Loss Modelling

The losses present in electromechanical devices can include core, winding (ac and dc), PM, aerodynamic and mechanical loss components, [20]. Due to the quasi-static operation of the actuator and the high-thrust-force, the dc winding loss, P_w, is assumed to be the dominant loss source and is estimated using (1).

$$P_w = \rho_c J_c^2 V_c \left(1 + \alpha \left(T_c - T_0\right)\right) \tag{1}$$

Where J_c, V_c, ρ_c, α, T_0 and T_c are the conductor current density, conductor volume, conductor electrical resistivity, temperature coefficient of resistance, ambient temperature and

the conductor temperature respectively. Other loss sources such as those associated with the mechanical bearing system or the core losses induced by the turn-on and turn-off transients are neglected in the presented study.

V. Thermal Modelling

Accurate thermal analysis is dependent on a number of factors, such as the use of a modelling method which is able to provide sufficient thermal field detail, the correct estimation and distribution of losses, accurate material and interface properties, an understanding of the likely construction methods, for example the use of slot-liner and shrink fitting, as well as careful predictions of the heat transfer in the air-gaps and from the device surfaces via convection and radiation mechanisms, [21]. In order to minimise the need for direct thermal model calibration, each contributing factor is addressed in turn.

A. Mesh Based TEC Modelling Method

The temperature profile of the actuator is predicted using a mesh based axisymmetric TEC model which is automatically constructed from a geometric and material description of the actuator, [10], [22]. When compared with more traditional manually constructed lumped parameter networks, with few nodes, the automated mesh based approach maintains short solution times while allowing superior thermal field resolution and reduced model construction and set up times as well as enabling the identification of hot-spot temperatures and their location.

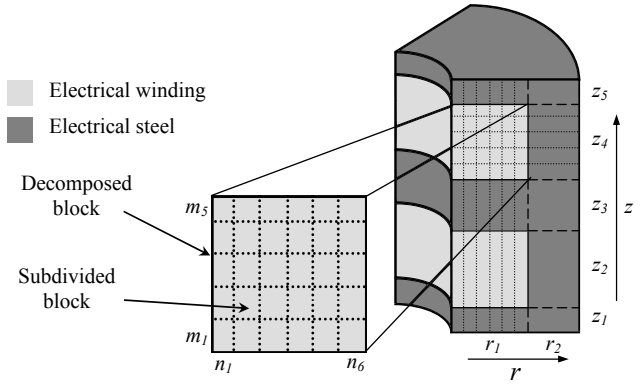

Fig. 2. Example of the discretisation of the actuator cross sectional geometry.

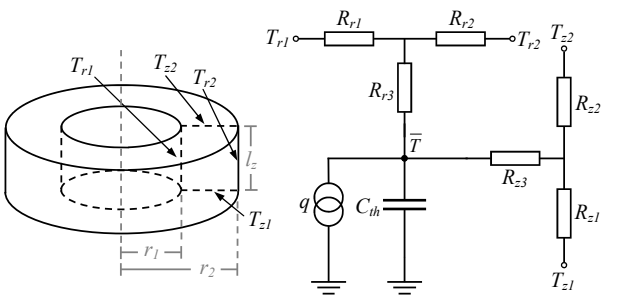

Fig. 3. Cylindrical TEC element.

The thermal model is generated by software which decomposes the actuator cross section geometry into a series of connected regular quadrilaterals, $(r_1, z_1) \rightarrow (r_n, z_n)$, which are further divided into $n \times m$ subregions as illustrated in Fig. 2. Each subdivided region is represented by a cylindrical TEC element, Fig. 3, which is formulated using T-networks to report the average temperature over the volume at the central node, $\bar{T}$, and caters for anisotropic thermal conductivity and internal heat generation, [23], [24]. In certain circumstances the T-network representation can be shown to overestimate temperature during transient simulations if a compensation method is not applied, [25]. However, this effect is mitigated in the present case by employing a sufficiently high number of subdivisions within the model, selected to provide a favourable trade-off between the thermal field detail, accuracy and computation time. Each cylindrical TEC element representing the winding regions contains a local loss model, implemented using a voltage (temperature) controlled current (loss) source, which emulates the scaling of distributed dc winding loss with temperature according to (1). The resulting TEC model is solved using a SPICE based circuit simulator, [26], and the nodal voltages (temperatures) are post-processed to extract the winding hot-spot temperature and location as a function of time.

B. Winding Design and Estimation of Equivalent Thermal Properties of the Impregnated Winding

A schematic of the selected winding configuration is illustrated in Fig. 4 and has a packing factor of approximately $60\ \%$. This figure accounts for the likely voids remaining between the conductors after manufacture resulting from the rounded edges of the conductor profile along with imperfect alignment and seating within the slot.

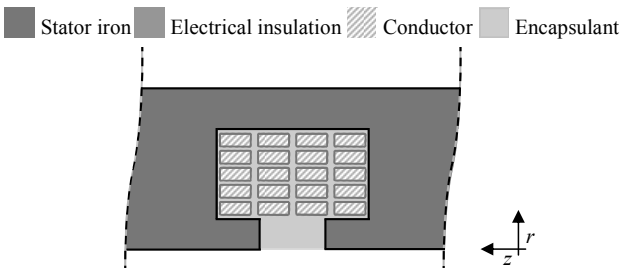

Fig. 4. Schematic of the actuator winding configuration.

The impregnated electrical winding is a composite material composed of conductors, conductor insulation and encapsulant insulation. Representing each material and associated geometry, often with disparate dimension scales, within a thermal model would add significant complexity and lead to long solution times. Therefore, following common practise, the winding is represented as a homogeneous anisotropic lumped region with equivalent thermal properties, [21], [27]. The equivalent thermal conductivity and specific heat capacity of the winding are estimated using a numerical FE model of the heat-flow

across a cuboidal section of the winding and an analytical expression based on the relative volume of the constituent materials, respectively. The estimation methods have been experimentally validated using measurements performed on winding samples similar to that illustrated in Fig. 5, [11]. The thermal properties of the actuator's constituent materials, as reported by the respective manufacturers, are given in Table II and are assumed to remain constant over the temperature range of interest (approximately 25 °C to 180 °C).

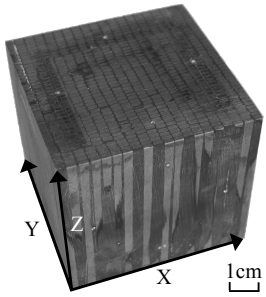

Fig. 5. An example of an epoxy impregnated winding sample, measuring 66 mm × 66 mm × 66 mm, with rectangular cross section conductors.

TABLE II
MATERIAL PROPERTIES

Material	Thermal Conductivity [W/m.K]	Specific Heat Capacity [J/m^3.K]	Density [kg/m^3]
Steel 316	16.3	500	8000
Somaloy 700	25	457	7540
Copper	385	386	8890
Polyamide-imide	0.26	1000	1440
Epoxy impregnation	0.85	1700	1766
SmCo Recoma 30s	10	350	8300

The relative volume of conductor and insulation materials within the actuator winding scales with the slot dimensions to give a constant packing factor, therefore, the estimated equivalent thermal properties are expected to remain constant over the range of slot dimensions investigated. However, the thermal property estimation methods presented in [11] assume that the winding is fully penetrated by the encapsulant insulation which is difficult to achieve in a practical device and is likely to contain imperfections.

The effect of imperfect impregnation is modelled by linearly varying the effective thermal properties of the encapsulant insulation in the FE model in proportion to a Winding Impregnation Quality factor, $IQ_{winding}$, between those of still air and those of pure encapsulant insulation. These extremes emulate a non-impregnated air filled winding, where convection currents are neglected, and a fully impregnated winding respectively. The effect of $IQ_{winding}$ on the equivalent thermal conductivity of the winding is illustrated in Fig. 6. In practise, the actuator winding is to be manufactured using vacuum impregnation and previous experience constructing practical devices has shown the impregnation quality, $IQ_{winding}$, to be approximately

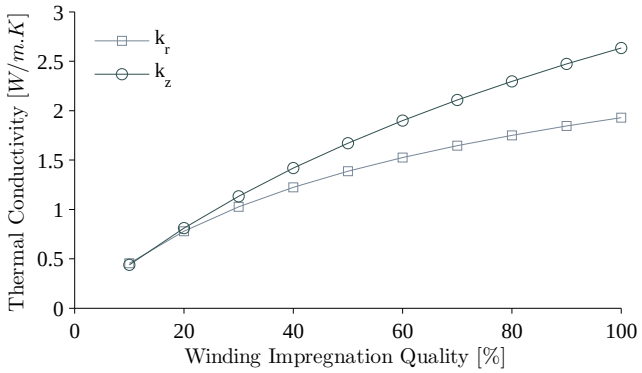

Fig. 6. Estimated axial and radial thermal conductivity of the actuator winding obtained from a two-dimensional thermal FE model.

60 % using the equipment available. The equivalent thermal properties of the actuator winding region are estimated using this information along with Table II and are given in Table III.

TABLE III
WINDING EQUIVALENT THERMAL PROPERTIES

Property	Value	Unit
Packing Factor	60	%
Winding Impregnation Quality	60	%
Thermal conductivity r-axis	1.5	W/m.K
Thermal conductivity z-axis	1.9	W/m.K
Specific heat capacity	344	J/kg.K
Density	8700	kg/m^3

C. Convection and Radiation Heat Transfer Coefficients

Heat transfer by convection and radiation mechanisms is assumed to be limited to the cylindrical outer surface of the actuator and across the mechanical air-gap. The heat transfer coefficients are estimated using published empirically derived heat transfer correlations, [28], and are a function of several physical actuator properties such as the surface temperature and the inner and outer stator diameter, governed by the split-ratio, r_o/r_i.

In order to simplify the analysis the following assumptions are made:

- the effector is static
- the average stator surface temperature is in the range $25 \leq T_s \leq 60$ °C
- the stator split ratio is 0.5

1) Surface Heat Transfer Coefficient:

$$h_{rsurf} = \frac{\epsilon\sigma\left(T_s^4 - T_0^4\right)}{T_s - T_0} \tag{2}$$

The surface radiation heat transfer coefficient, h_{rsurf}, is determined to lie in the range $3.6 \leq h_{rsurf} \leq 4.3$ W/m^2.K from (2) where, ϵ, σ, T_s and T_0 are the surface emissivity, taken as 0.6 for the machined Somaloy SMC components, the Stefan-Boltzmann constant and the surface and ambient temperatures (in Kelvin) respectively, [29].

$$h_c = \frac{k_{air}}{D}\left[0.6 + \frac{0.387 Ra_D^{\frac{1}{6}}}{\left[1+\left(\frac{0.559}{Pr}\right)^{\frac{9}{16}}\right]^{\frac{8}{27}}}\right]^2 \quad (3)$$

The natural convection heat transfer coefficient from the surface, h_{csurf}, is estimated to lie in the range $3.6 \leq h_{csurf} \leq 4.4$ W/m^2.K using the Churchill and Chu correlation for a horizontal cylinder, [30], (3). Here the heat transfer is defined in terms of the thermal conductivity of still air, k_{air}, the diameter of the stator, D, and the dimensionless Rayleigh, $Ra_D = 9.1 \times 10^5$, and Prandtl, $Pr = 0.73$, numbers. The radiation and convection heat transfer coefficients are summed to represent the heat transfer mechanisms occurring in parallel resulting in an average combined heat transfer coefficient of $h_{surf} = h_{rsurf} + h_{csurf} = 8.0$ W/m^2.K.

2) Air-gap Heat Transfer Coefficient:

$$h_{rag} = \frac{1}{T_e - T_s}\frac{\sigma\left(T_e^4 - T_s^4\right)}{\frac{1}{\epsilon_e} + \frac{1-\epsilon_s}{\epsilon_s}\left(\frac{r_e}{r_s}\right)} \quad (4)$$

The radiation heat transfer coefficient across the mechanical air-gap, Fig. 1, is estimated using a relation applicable to concentric cylinders, (4), where the subscripts s and e refer to the stator inner bore and the effector respectively. The emissivity of the inner stator bore and effector surface are assumed to be equal resulting in an average radiation heat transfer coefficient of $h_{rag} = 3.1$ W/m^2.K, Table I.

$$k_{eff} = k_{air} 0.386 \left[\frac{Pr}{0.861 + Pr}\right]^{1/4} \left(F_{cyl} Ra_L\right)^{1/4} \quad (5)$$

The equivalent thermal conductivity of the air-gap which includes the effects of natural convection is estimated using a correlation proposed by Raithby and Hollands, [31], (5), where F_{cyl} is a geometric factor. The natural convection currents are considered negligible if $F_{cyl} Ra_L < 100$ and is shown to be the case in this analysis ($Pr = 0.73$, $Ra_L = 0.34$) over the range of geometric dimensions of interest. Therefore, $k_{eff} = k_{air}$ giving an equivalent convection heat transfer coefficient of $h_{cag} = 3.5$ W/m^2.K. Hence, a combined convection and radiation heat transfer coefficient of $h_{ag} = h_{cag} + h_{rag} = 6.6$ W/m^2.K is applied to the air-gap region.

D. Material Interface Gaps and Thermal Contact Resistance

The interface gaps between machine components such as the stator and casing manifest as contact thermal resistances and can significantly impede heat flow, they are caused by surface imperfections and are influenced by factors such as material hardness, surface roughness and interface pressure, [21], [32]. In the present study the number of interface gaps is minimised since the actuator is not fitted with a case and the stator is thermally isolated from the test-rig in order to render the heat sinking effect negligible and maintain well defined test conditions. The interface gaps that exist between the axially segmented stator sections are filled and bonded using thermally conductive epoxy to minimise the interface thermal resistance.

VI. Overview of Design Methodology

A. Design Methodology Structure

Due to the quasi-static operation and high-thrust-force of the actuator the dc winding loss is assumed to be the sole loss source, Section IV, and can be determined analytically based on the winding current demand, (1), independently of the electromagnetic model. Hence, the electromagnetic and thermal models are regarded as being loosely coupled and the dc winding loss is calculated and updated with temperature locally within the TEC model, Section V-A. This arrangement not only minimises the number of electromagnetic FE evaluations but enables the models to be analysed in parallel. For example, the cogging-force-displacement and thrust-force-displacement profile of the actuator are found by evaluating a series of independent magnetostatic FE models at various effector displacements and winding current demands. This set of FE analyses can be performed in parallel alongside the thermal model analysis, and is achieved using a simple queueing algorithm designed to control the execution timing of the models and take advantage of modern multi-core desktop computing hardware, thereby minimising the computation time of the multi-physics analysis.

The structure of the proposed design methodology is illustrated in Fig. 7. An initial design parameter set, D_{pi}, Table IV, material properties, Tables II and III and heat transfer coefficients, Section V-C, are passed to a parametric model of the actuator cross sectional geometry. This data and geometry are then passed to the magnetostatic and thermal models which are evaluated in parallel. The resulting actuator performance information, such as the winding temperature rise and the thrust force capability of the design is passed to an objective function, $E\left(D_p\right)$, Section VII-A, which returns a numeric indicator of the actuator performance with respect to the desired specification, Section II.

An iterative optimisation routine repeats the analysis process, perpetually modifying the slot geometry and electric loading, Fig. 8 and Table IV, and evaluating the resulting design performance until an optimal design parameter set is identified in which the design meets the specification i.e. the objective function is minimised, or a stopping criteria such as a maximum number of iterations is exceeded.

B. Optimisation Algorithm Selection

The selection of an optimisation algorithm results in a trade-off between the ease of implementation, applicability, convergence time, the reliability of the method when applied to a black-box problem, the level of user interaction required and the quality of the resulting optimum, [33]. The Particle Swarm Optimisation (PSO) algorithm is selected in the present case as it has been application proven in the design of electrical machines and wound passive components, [4], [34], and exhibits several advantageous features, [35]:

- continuous and discrete objective function handling

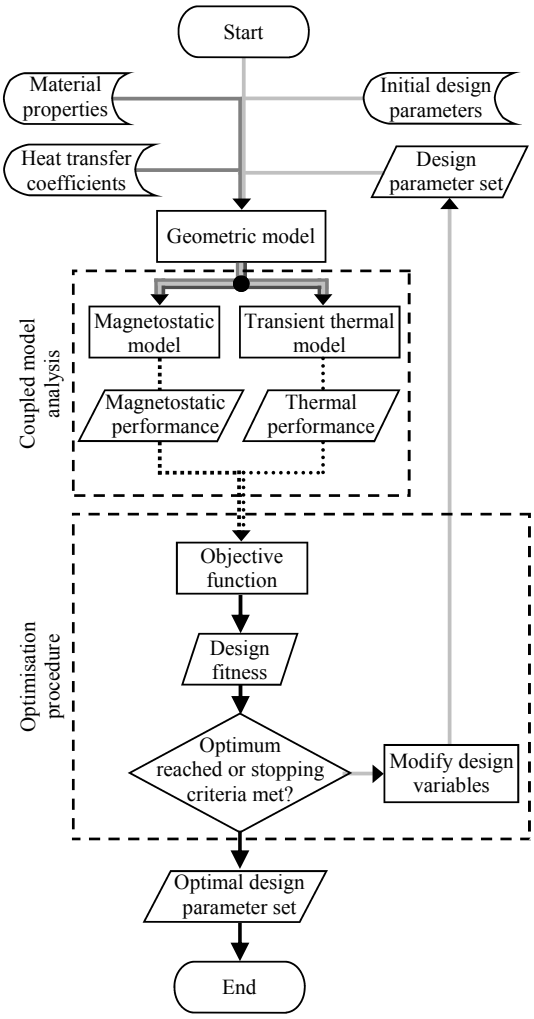

Fig. 7. An overview of the design methodology used to design a short-duty high-force-density tubular linear actuator.

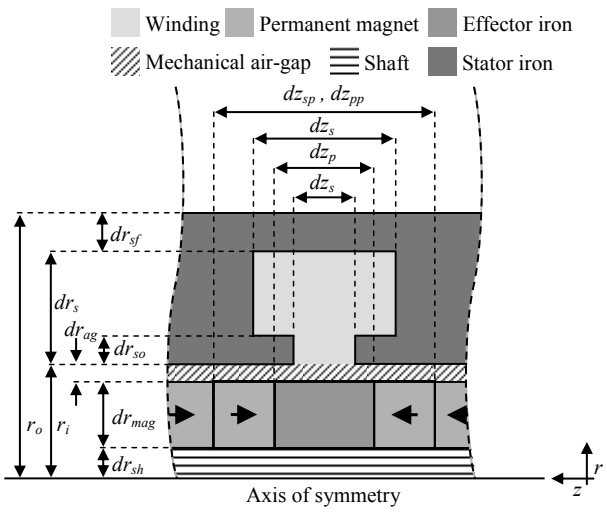

Fig. 8. Actuator slot cross section geometry.

TABLE IV
ACTUATOR DESIGN VARIABLES.

Symbol	Description	Value/Range
dz_{sp}	stator slot pitch	$0 > dz_{sp} \leq l_s$
dz_{pp}	effector pole pitch	$0 > dz_{pp} \leq l_s$
N_s	number of stator slots	$1 \geq N_s \leq 6$
N_p	number of effector poles	$1 \geq N_p \leq 6$
r_i/r_o	stator split-ratio	$0 > r_i/r_o < 1$
dr_{mag}/dr_{sh}	magnet radial thickness to shaft radius ratio	$0 > dr_{mag}/dr_{sh} < 1$
dz_s/dz_{sp}	slot width to slot pitch ratio	$0 > dz_s/dz_{sp} < 1$
dz_p/dz_{pp}	pole width to pole pitch ratio	$0 > dz_p/dz_{pp} < 1$
dz_{so}/dz_s	slot opening width to slot width ratio	$0 > dz_{so}/dz_s < 1$
dr_{so}/dr_s	tooth-tip thickness to slot depth ratio	$0 > dr_{so}/dr_s < 1$
J_w	winding current density	$0 > J_w \leq 60$ A/mm^2

- linear and non-linear constraint handling
- relatively simple implementation
- global optimisation, typically unaffected by local extrema
- requires minimal to no user interaction during operation

VII. Application of Design Methodology

The actuator slot geometry, Fig. 8, is parametrically defined using dimension ratios, Table IV, enabling a vector of design variables in the range $0 \rightarrow 1$ to fully describe a physically valid slot geometry within the space envelope, Table I. Additional design variables are the winding current density (electric loading) and the number of slots and poles. The actuator is similar to a Linear Oscillating Actuator (LOA) in nature where a favourable relationship between the number of teeth, N_t, and the number of effector poles, N_p, is $|N_t - N_p| = 1$, [36]. Considering the constrained space envelope, it is desirable to minimise the effector overhang with respect to the stator, therefore, an equal number of stator slots and effector poles of $N_s = N_p = 4$ is assumed which gives a good compromise between performance and manufacturability.

A. Objective Function Definition

The objective function can be formulated in a number of different ways, however, an appropriate form in this instance is to treat the effector output force, F, duty, t, and maximum operating temperature, T_{max} as design targets and represent them as a weighted sum of normalised error terms, (6), where $E\left(D_p\right)$ returns zero for a design which meets the desired specification. The subscripts c and t refer to the current and the target actuator design performance respectively. The objective function contains two additional terms which ensure that the cogging-force-displacement profile is monotonic, linear and of the correct sense to provide a restoring force on the effector. To determine the linearity of the profile it is fitted to a first order polynomial and the coefficient of determination, $\mathbf{R^2}$, which returns 0 for a low correlation and 1 for a high correlation is found. The sense of the restoring force is determined from the gradient of the cogging-force-displacement profile at zero displacement, df_{co}/dx, and is formulated into an objective function term which returns 0 for the correct force sense. The

weights, W_F, W_t, $W_{T_{max}}$ and $W_{\mathbf{R^2}}$ are empirically selected based on the observed convergence of the optimisation routine.

$$\begin{aligned} E\left(D_p\right) = W_F \left|\frac{F_t - F_c\left(D_p\right)}{F_t}\right| \\ + W_t \left|\frac{t_t - t_c\left(D_p\right)}{t_t}\right| \\ + W_{T_{max}} \left|\frac{T_{maxt} - T_c\left(D_p\right)}{T_{maxt}}\right| \\ + W_{\mathbf{R^2}} \left|1 - \mathbf{R^2}\left(D_p\right)\right| \\ + \left|1 + \frac{\frac{df_{co}}{dx}\big|_{x=0}}{\left|\frac{df_{co}}{dx}\big|_{x=0}\right|}\right| \end{aligned} \tag{6}$$

B. Design Results

The PSO employs a random factor in the selection of design parameters which can affect the outcome of the optimisation process. In addition, the objective function formulation effectively combines multiple design objectives into a single, non-unique function, hence a set of designs exist which can be considered equally optimal with respect to the objective function but exhibit varying geometries and characteristics representing a range of compromises between the individual design objectives. To appraise the impact of the random nature of the PSO and the adopted objective function formulation, the design methodology is executed on three separate desktop computers and the results compared.

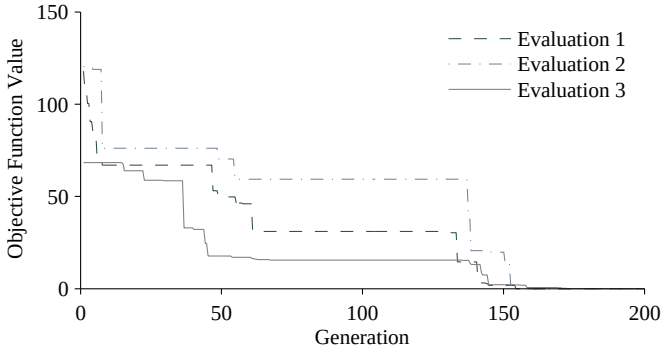

Fig. 9. Objective function value as a function of optimisation iteration for three independent design methodology evaluations.

Fig. 9 shows the objective function value, (6), as a function of the PSO generation for each design methodology evaluation. It is evident that the random factor in the optimisation routine leads to differing search paths through the design space, however, convergence is reached in an average of 150 generations in each case with an average objective function value of 0.05. It is found in this instance that the three design methodology evaluations show negligible variation in the resulting design variable sets, D_p, therefore, the set corresponding with the lowest objective function value is selected. The similarity between the optimised designs could be attributed to the highly constrained problem exhibiting a small feasible region. However, if the design methodology were evaluated many more times, alternative design solutions may be identified.

The final design parameter set which meets the specification is given in Table V along with a table of performance metrics, Table VI. The average computation time of the design methodology was approximately 50 hours with 9 bounded design variables, Table IV. In practise the computation time is highly dependent on the number of design variables, the size of the search space and the rate of convergence which can be slow for highly constrained problems, as in this case.

TABLE V
FINAL ACTUATOR DESIGN VARIABLES.

Symbol	Description	Value
dz_{sp}	stator slot pitch	26 mm
dz_{pp}	effector pole pitch	26 mm
N_s	number of stator slots	4
N_p	number of effector poles	4
r_i/r_o	stator split-ratio	0.54
dr_{mag}/dr_{sh}	magnet radial thickness to shaft radius ratio	0.45
dz_s/dz_{sp}	slot width to slot pitch ratio	0.54
dz_p/dz_{pp}	pole width to pole pitch ratio	0.58
dz_{so}/dz_s	slot opening width to slot width ratio	0.23
dr_{so}/dr_s	tooth-tip thickness to slot depth ratio	0.35
J_w	winding current density	49.4 A/mm^2

TABLE VI
ACTUATOR DESIGN PERFORMANCE.

Metric	Value	Units
Peak winding temperature @ $t = 32$ s	175	^{o}C
Average winding temperature @ $t = 32$ s	133	^{o}C
Average surface temperature @ $t = 32$ s	52	^{o}C
Rated winding current	206	A
Peak conductor current density	49.4	A/mm^2
Peak slot current density	29.2	A/mm^2
Short-duty force-density	$1.6 - 3.8$	N/cm^3
Air-gap shear stress	$67 - 153$	kPa
Maximum thrust force	2203	N
Minimum thrust force	964	N
Average thrust force	1766	N

The effect of the optimisation procedure on the evolution of the actuator design is illustrated in Fig. 10 where Fig. 10a is the cross section of an initial actuator design taken from generation 1 of the PSO and Fig. 10b is the cross section of the optimised actuator design, Table V. The tooth-tip thickness, tooth shank thickness and slot openings of the optimised design are increased by 68 %, 60 % and 50 % respectively. This results in a design with lower open circuit saturation that is more mechanically robust but has a 38 % reduction in slot area and 40 % reduction in slot volume. In order to partially compensate for the lower slot volume, the slot current

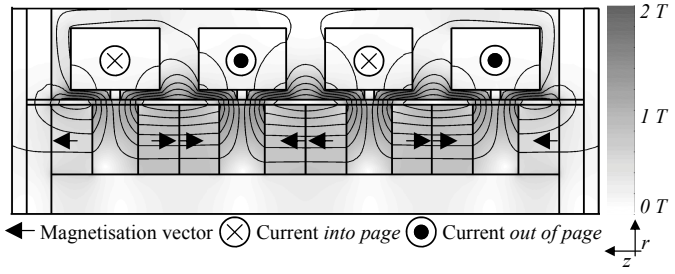

(a) Example initial actuator design.

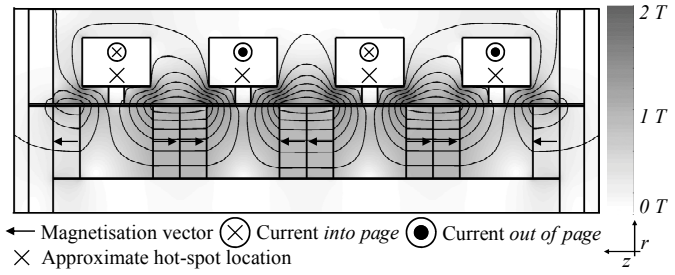

(b) Optimised actuator design.

Fig. 10. Comparison of the optimised $N_s = N_p = 4$ actuator cross sectional geometry with a design from the initial PSO population with the effector at 0% displacement.

density, J_s, is 7.5 % higher and results in a winding loss that is 16 % higher at the ambient temperature since the winding loss is proportional to ${J_s}^2 V_s$ where V_s is the slot volume. In the steady-state the additional winding loss would have a significant impact on the actuator temperature, however, in the short-duty case the increased heat capacity of the 38 % higher stator core volume acts as a heat sink and makes the short-duty thermal performance of the two designs comparable. At the end of the 32 s transient, the predicted peak winding temperature of the initial and optimised design reaches 180 °C and 175 °C respectively. The PM material in the optimised design is reduced by 34 % and the the air-gap area of both designs is within 2 %.

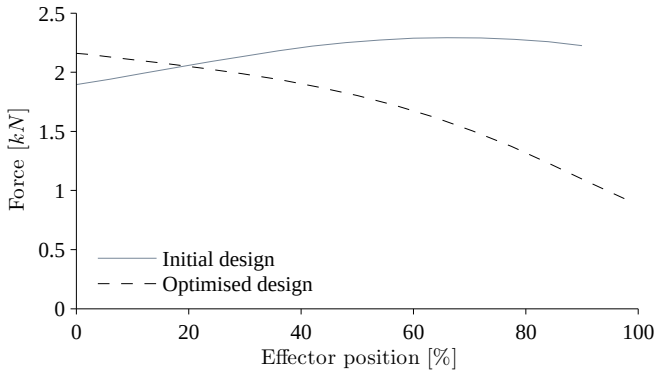

Fig. 11. Comparison of the thrust-force-displacement profiles of an initial design candidate and the optimised design obtained assuming a constant dc current in each coil.

Both of the designs exhibit an average thrust force of

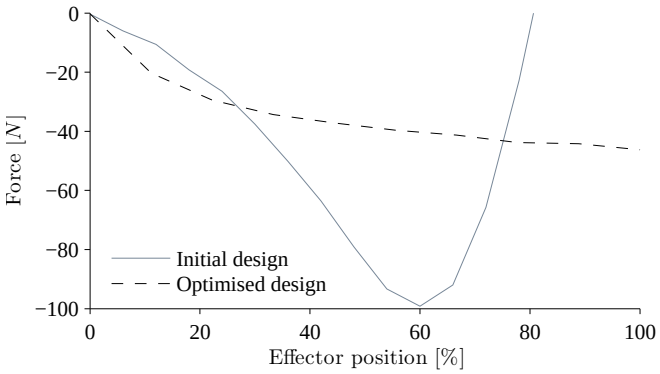

Fig. 12. Comparison of the cogging-force-displacement profiles of an initial design candidate and the optimised design.

$\geq$ 1.5 kN over the effector displacement. The thrust force profile of the initial design steadily increases up to an effector displacement of 50 % where the profile plateaus, Fig. 11. The optimised design has a 16 % higher thrust force at low displacements, however, the thrust force reduces rapidly as a function of effector displacement which is attributed to the increased saliency of the effector caused by the lager iron segment dimension, Fig. 1 and Fig. 10b. The initial design has a cogging force magnitude over 2 times greater than that of the optimised design, Fig. 12, however, the profile is not monotonic, with an inversion at an effector displacement of 60 %. Hence the initial design cannot provide a consistent restoring force over the full effector displacement and is therefore an undesirable design, whereas, the cogging force of the optimised design is monotonic and of the correct sense to provide the required effector restoring force owing to the wider tooth shank and higher slot opening height which reduces the saturation of the tooth-tips.

An assessment of the risk of PM demagnetization of the actuator design is performed as a post-optimisation step under the worst case winding excitation and predicted PM temperature. The assessment shows that PM demagnetisation is not a risk over the displacement and excitation range of the design. Detailed mechanical design aspects were not considered within the automated design methodology, hence, the suitability and stiffness of the shaft was evaluated and appropriate bearings selected manually as a further post-optimisation step.

VIII. Prototype Actuator Construction and Testing

In order to validate the electromagnetic and thermal predictions of the coupled design methodology, a prototype actuator was constructed and tested. Fig. 13 illustrates the winding and construction of individual stator slots where each slot is formed from two machined Somaloy 700 SMC segments. Each segment contains a double layer winding which enables a good conductor fill to be achieved whilst remaining simple to manufacture and allows the stator segments to be wound independently and terminated externally, Section VIII and Fig. 13.

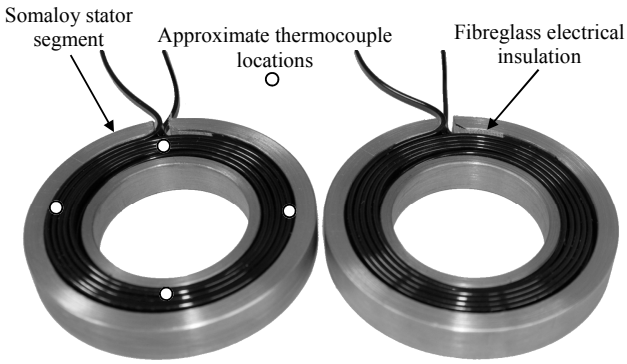

Fig. 13. Wound stator segments.

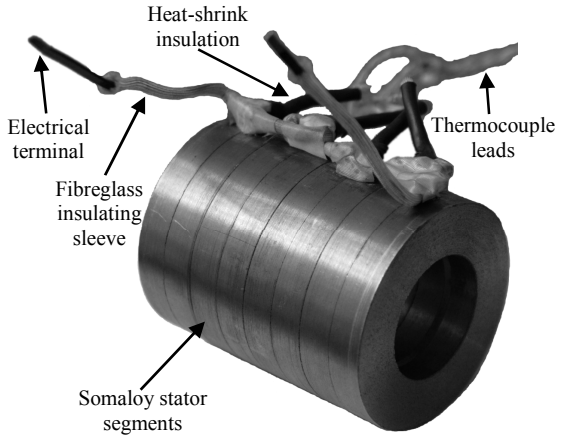

Fig. 14. Actuator stator.

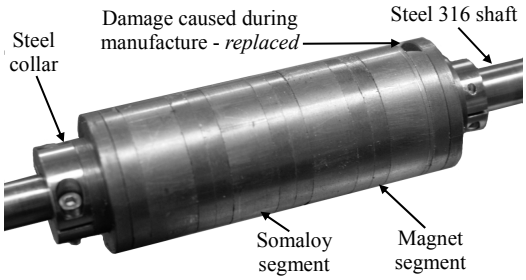

Fig. 15. Actuator effector.

Four individual stator slots are bonded using thermally conductive epoxy to form the full actuator stator, Fig. 14. The complete actuator effector is illustrated in Fig. 15 and is composed of alternate PM and Somaloy SMC segments abutted by aluminium end plates and steel collars set into grooves in the steel 316 shaft.

The stator and effector components are assembled, aligned and mounted on a test-rig, Fig. 16, which is designed to maintain the mechanical integrity of the actuator without the need for a stator housing which will be required in the final application. The test rig features a precision barrel adjuster, linear displacement sensor (LDS1103) and a linear force transducer (TEDEA 615), Fig. 17, to enable the effector displacement and force to be measured accurately.

The actuator is subjected to short-duty dc tests at winding current levels ranging from 50 A to 200 A (below the rated 206 A to provide a margin for error) in 25 A increments between effector displacements of 0 mm to 5 mm at 0.5 mm increments. The winding current is supplied by a dc power supply (EA-PS 8080-510) through a time controlled contactor and measured using a precision current transducer (LEM IT400-S). Type K thermocouples are distributed over the actuator surface and are embedded within the winding slots, Figs. 13 and 16. The dc winding power, actuator temperature rise and the effector thrust force are recorded by a data acquisition system at 0.2 s intervals (Agilent 34972A).

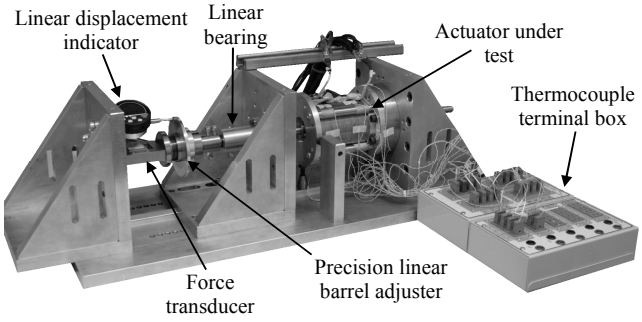

Fig. 16. Actuator test rig.

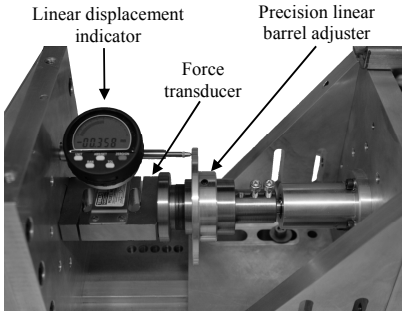

Fig. 17. Effector linear position adjuster.

IX. Experimental Results

Fig. 18 presents the measured and predicted effector cogging-force-displacement profile. The measured data is plotted with error bars indicating the combined stated error of the load cell and the strain gauge amplifier. The measured data shows close correlation with the predicted values. The small variation is explained by the mechanical tolerances of the physical components and the difficulty in repeating measurements with the load cell under tension and compression.

Fig. 19 presents the measured and predicted effector thrust force as a function of displacement and winding current. The measured data shows a close correlation with the predicted values for winding current levels up to 150 A. At winding current levels of $150 - 200A$, the model overpredicts the

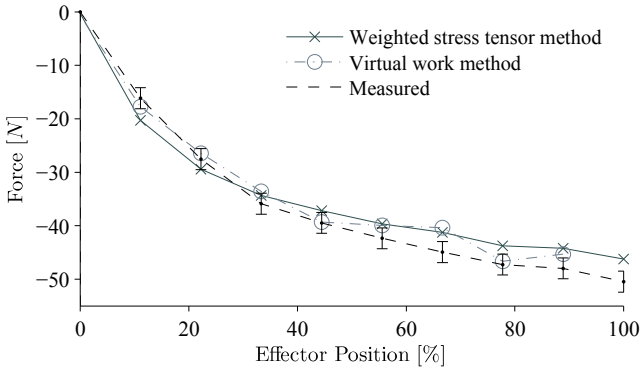

Fig. 18. Effector cogging-force-displacement profile.

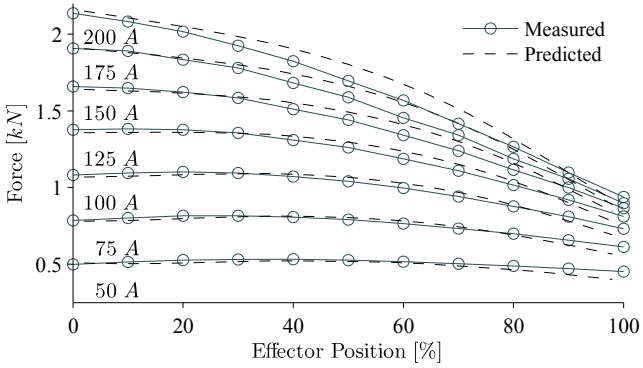

Fig. 19. Effector thrust-force-displacement profile.

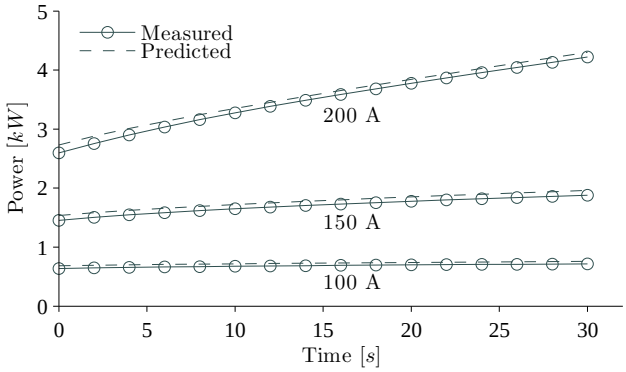

Fig. 20. Actuator dc winding loss evolution with time.

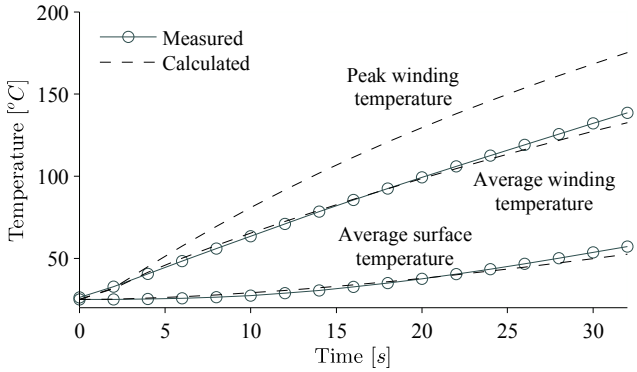

Fig. 21. Actuator temperature evolution with time.

effector thrust with the largest error occurring in the mid range of effector position. The agreement between the measured and predicted values at relatively low winding current levels suggests that the material data used in the magnetostatic model are accurate. A potential source of error is the reluctance force component exhibited by the IPM arrangement being greater than expected. This could be caused by mechanical tolerance and alignment of the components. Alternatively the error could stem from the remnant flux density of the PMs reducing throughout the experiments as a result of temperature drift. The stator and effector are cooled between each experiment, however, due to the small physical size of the mechanical air-gap, the magnet temperature could not be directly measured to ensure that they remain at a consistent temperature.

Fig. 20 presents the measured and predicted winding loss which are in close agreement over the transient, this shows that the local loss model within the TEC model is well defined and indirectly indicates that the predicted temperature rise of the winding is accurate. Fig. 21 presents the measured and predicted temperature rise of the actuator surface and the windings over time. As the peak winding temperature is not accessible for direct measurement, Fig. 10b, the predicted temperature trajectory with a peak of 175 °C is shown. The average winding and average surface temperatures show close correlation over the duration of the test which indicates that the thermal model is well formulated and gives further confidence in the peak winding temperature prediction.

X. Conclusion

This paper proposes a coupled electromagnetic and thermal design methodology applied to a high-force-density linear actuator intended for infrequent short-duty operation. The choice of methodology structure, modelling techniques and model coupling are intended to minimise the overall computation time required to optimise a design.

In order to validate the design methodology and modelling techniques, a prototype actuator is constructed and subjected to a series of short-duty tests. The cogging-force-displacement, thrust-force-displacement and temperature predictions show close agreement with the predicted performance. The results demonstrate that a short-duty device can be designed to operate close to the thermal limit of the insulation materials without the need for direct thermal model calibration within a reasonable time-frame using modern desktop computing hardware.

The proposed design methodology serves as a good first step in the development of a more general accurate and computationally efficient multi-physics design methodology applicable to electrical machines and wound passive components. However, the present application is a comparatively simple case of a wide range of electrical machine types and topologies.

A more comprehensive approach would additionally need to cater for:

- frequency, current and temperature dependent loss sources such as ac winding loss and core loss
- interface gaps, specifically between the windings and the iron and between the casing and the machine
- surface, air-gap and end-space heat transfer coefficients for a range of cooling types
- quantifiable build factors

These additional features are not trivial to investigate or implement, particularly whilst maintaining a low computation time for a design optimisation, therefore an opportunity for substantial future work exists.

REFERENCES

[1] A. Boglietti, A. Cavagnino, D. Staton, M. Shanel, M. Mueller, and C. Mejuto, "Evolution and modern approaches for thermal analysis of electrical machines," *Industrial Electronics, IEEE Transactions on*, vol. 56, no. 3, pp. 871–882, 2009.

[2] P.-D. Pfister and Y. Perriard, "Very-high-speed slotless permanent-magnet motors: Analytical modeling, optimization, design, and torque measurement methods," *Industrial Electronics, IEEE Transactions on*, vol. 57, no. 1, pp. 296–303, 2010.

[3] Z. Makni, M. Besbes, and C. Marchand, "Multiphysics design methodology of permanent-magnet synchronous motors," *Vehicular Technology, IEEE Transactions on*, vol. 56, no. 4, pp. 1524–1530, 2007.

[4] N. Bracikowski, M. Hecquet, P. Brochet, and S. Shirinskii, "Multiphysics modeling of a permanent magnet synchronous machine by using lumped models," *Industrial Electronics, IEEE Transactions on*, vol. 59, no. 6, pp. 2426–2437, 2012.

[5] L. Encica, J. J. H. Paulides, E. Lomonova, and A. J. A. Vandenput, "Electromagnetic and thermal design of a linear actuator using output polynomial space mapping," *Industry Applications, IEEE Transactions on*, vol. 44, no. 2, pp. 534–542, 2008.

[6] I. Vese, F. Marignetti, and M. Radulescu, "Multiphysics approach to numerical modeling of a permanent-magnet tubular linear motor," *Industrial Electronics, IEEE Transactions on*, vol. 57, no. 1, pp. 320–326, 2010.

[7] W. Jiang and T. Jahns, "Development of efficient electromagnetic-thermal coupled model of electric machines based on finite element analysis," in *Electric Machines Drives Conference (IEMDC), 2013 IEEE International*, 2013, pp. 816–823.

[8] T. Hamiti, C. Gerada, and M. Rottach, "Weight optimisation of a surface mount permanent magnet synchronous motor using genetic algorithms and a combined electromagnetic-thermal co-simulation environment," in *Energy Conversion Congress and Exposition (ECCE), 2011 IEEE*, 2011, pp. 1536–1540.

[9] Y. Wang, D. Ionel, and D. Staton, "Ultrafast steady-state multi-physics model for pm and synchronous reluctance machines," *Industry Applications, IEEE Transactions on*, vol. PP, no. 99, pp. 1–1, 2015.

[10] N. Simpson, R. Wrobel, and P. Mellor, "An accurate mesh-based equivalent circuit approach to thermal modeling," *Magnetics, IEEE Transactions on*, vol. 50, no. 2, pp. 269–272, Feb 2014.

[11] ——, "Estimation of equivalent thermal parameters of impregnated electrical windings," *Industry Applications, IEEE Transactions on*, vol. 49, no. 6, pp. 2505–2515, Nov 2013.

[12] J. Eastham, R. Akmese, and H. Lai, "Optimum design of brushless tubular linear machines," *Magnetics, IEEE Transactions on*, vol. 26, no. 5, pp. 2547–2549, Sep 1990.

[13] J. Wang, D. Howe, and Z. Lin, "Design optimization of short-stroke single-phase tubular permanent-magnet motor for refrigeration applications," *Industrial Electronics, IEEE Transactions on*, vol. 57, no. 1, pp. 327–334, Jan 2010.

[14] J. Wang and D. Howe, "Influence of soft magnetic materials on the design and performance of tubular permanent magnet machines," *Magnetics, IEEE Transactions on*, vol. 41, no. 10, pp. 4057–4059, Oct 2005.

[15] X. Chen, Z. Zhu, D. Howe, and J. Dai, "Comparative study of alternative permanent magnet linear oscillating actuators," in *Electrical Machines and Systems, 2008. ICEMS 2008. International Conference on*, Oct 2008, pp. 2826–2831.

[16] M. Yilmaz and P. Krein, "Capabilities of finite element analysis and magnetic equivalent circuits for electrical machine analysis and design," in *Power Electronics Specialists Conference, 2008. PESC 2008. IEEE*, June 2008, pp. 4027–4033.

[17] N. Bianchi, "Analytical field computation of a tubular permanent-magnet linear motor," *Magnetics, IEEE Transactions on*, vol. 36, no. 5, pp. 3798–3801, Sep 2000.

[18] N. Bianchi, S. Bolognani, and F. Tonel, "Design criteria of a tubular linear ipm motor," in *Electric Machines and Drives Conference, 2001. IEMDC 2001. IEEE International*, 2001, pp. 1–7.

[19] D. Meeker, "Femm 4.2," http://www.femm.info/, 2013.

[20] R. Wrobel, D. Salt, A. Griffo, N. Simpson, and P. Mellor, "Derivation and scaling of ac copper loss in thermal modeling of electrical machines," *Industrial Electronics, IEEE Transactions on*, vol. 61, no. 8, pp. 4412–4420, Aug 2014.

[21] A. Boglietti, A. Cavagnino, and D. Staton, "Determination of critical parameters in electrical machine thermal models," *Industry Applications, IEEE Transactions on*, vol. 44, no. 4, pp. 1150–1159, 2008.

[22] F. Qi, A. Stippich, M. Guettler, M. Neubert, and R. De Doncker, "Methodical considerations for setting up space-resolved lumped-parameter thermal models for electrical machines," in *Electrical Machines and Systems (ICEMS), 2014 17th International Conference on*, Oct 2014, pp. 651–657.

[23] P. Mellor, D. Roberts, and D. Turner, "Lumped parameter thermal model for electrical machines of tefc design," *Electric Power Applications, IEE Proceedings B*, vol. 138, no. 5, pp. 205–218, 1991.

[24] R. Wrobel and P. Mellor, "A general cuboidal element for three-dimensional thermal modelling," *Magnetics, IEEE Transactions on*, vol. 46, no. 8, pp. 3197–3200, 2010.

[25] D. Kuehbacher, A. Kelleter, and D. Gerling, "An improved approach for transient thermal modeling using lumped parameter networks," in *Electric Machines Drives Conference (IEMDC), 2013 IEEE International*, May 2013, pp. 824–831.

[26] P. Nenzi and H. Vogt, "Ngspice 26," http://ngspice.sourceforge.net/, 2013.

[27] D. Staton, A. Boglietti, and A. Cavagnino, "Solving the more difficult aspects of electric motor thermal analysis in small and medium size industrial induction motors," *Energy Conversion, IEEE Transactions on*, vol. 20, no. 3, pp. 620–628, Sept 2005.

[28] D. Staton and A. Cavagnino, "Convection heat transfer and flow calculations suitable for electric machines thermal models," *Industrial Electronics, IEEE Transactions on*, vol. 55, no. 10, pp. 3509–3516, Oct 2008.

[29] Y. A. Cengel, *Heat & mass transfer: a practical approach*. Tata McGraw-Hill Education, 2007.

[30] S. W. Churchill and H. H. Chu, "Correlating equations for laminar and turbulent free convection from a horizontal cylinder," *International Journal of Heat and Mass Transfer*, vol. 18, no. 9, pp. 1049–1053, 1975.

[31] G. D. Raithby and K. G. T. Hollands, "A general method of obtaining approximate solutions to laminar and turbulent free convection problems," *Advances in Heat Transfer*, vol. II, pp. 265–315, 1975.

[32] D. Kulkarni, G. Rupertus, and E. Chen, "Experimental investigation of contact resistance for water cooled jacket for electric motors and generators," *Energy Conversion, IEEE Transactions on*, vol. 27, no. 1, pp. 204–210, March 2012.

[33] C. Boccaletti, S. Elia, and E. Nistico, "Deterministic and stochastic optimisation algorithms in conventional design of axial flux pm machines," in *Power Electronics, Electrical Drives, Automation and Motion, 2006. SPEEDAM 2006. International Symposium on*, May 2006, pp. 111–115.

[34] A. Sarikhani and O. Mohammed, "A multi-physics multi-objective optimal design approach of pm synchronous machines," in *Electrical Machines (ICEM), 2014 International Conference on*, Sept 2014, pp. 968–974.

[35] R. Poli, J. Kennedy, and T. Blackwell, "Particle swarm optimization," *Swarm Intelligence*, vol. 1, pp. 33–57, 2007.

[36] X. Chen, Z. Zhu, and D. Howe, "Modeling and analysis of a tubular oscillating permanent-magnet actuator," *Industry Applications, IEEE Transactions on*, vol. 45, no. 6, pp. 1961–1970, Nov 2009.